In-vivo tracking of harmonic nanoparticles: a study based on a TIGER widefield microscope [Invited]

Laura Vittadello,[1,2] **Christian Kijatkin**,[1,2] **Jan Klenen**,[1,2]
Dustin Dzikonski,[1,2] **Karsten Kömpe**,[2,3] **Christian Meyer**,[3]
Achim Paululat,[2,3] **and Mirco Imlau**[1,2,*]

[1]*Department of Physics, Osnabrück University, 49076 Osnabrück, Germany*
[2]*Center of Cellular Nanoanalytics, Osnabrück University, 49076 Osnabrück, Germany*
[3]*Department of Biology/Chemistry, Osnabrück University, 49076 Osnabrück, Germany*
*mirco.imlau@uni-osnabrueck.de

Abstract: *In vivo* tracking of harmonic nanoparticles (HNPs) in living animals is a technique not yet exploited, despite the great potential offered by these markers, due to a lack of an appropriate tool. The main drawback is the necessity to excite nonlinear effects in the millimeter area in a widefield mode with a sufficient signal to noise ratio. Our approach to this problem consists in a redesign of the laser space parameters in a region of high energy per pulse and low repetition rate in the kHz regime, in counter-trend with the actual microscope research technology. We realise this by means of a regeneratively amplified fs-laser system, creating an easy alignable and reproducible Tunable hIGh EneRgy (TIGER) widefield microscope. This one is successfully applied for HNPs tracking in the blood flow of the heart system of a *Drosophila* larvae, a powerful platform to study socially relevant diseases, such as congenital heart defects in human beings. It is possible to follow nonlinear emitting marker in a remarkable field-of-view of up to 1.5×1.5 mm^2 at 70 frame per seconds. The impact of the energy per pulse, the pulse repetition rate as well as of the photon energy on the SNR is determined and the optimum setup conditions are deduced. At the same time, wavelengths of fundamental and harmonic pulses are carefully considered and tailored to match the transmission fingerprint of the *Drosophila* larvae. Our findings clearly demonstrate the large impact of precise pulse parameter management in the view of the optical features of the sample, the optical setup and the photosensitivity of the detector. A step-by-step instruction for more general use of the technique is described, opening the path for addressing biological research questions that require far-field imaging at high frame rates with exceedingly high spatial and temporal precision.

1. Introduction

The possibility of using polar ferroelectric harmonic nanoparticles (HNPs) [1] for imaging in deep-tissue nonlinear optical (or multi-photon) microscopy [2] was first demonstrated by the research group of Demetri Psaltis in 2009 [3]. The approach comprises two major advantages: (i) the emission wavelength from HNPs can be tuned in the same sample from the ultraviolet (UV) to the near-infrared (NIR) spectral range without any gap [4,5]. This enables optimization of the signal-to-noise ratio as endogenous absorption can be avoided. At the same time, tissue damage can be suppressed efficiently. (ii) Multiple scattered signal photons can be assigned to their origin as the result of localized nonlinear signal generation. This enables 3D-imaging with high spatial resolution. HNP-based NLO microscopy extends the wide field of NLO imaging techniques using agents, such as nonlinear ultrasound imaging using bubbles [6,7].

In recent years, remarkable achievements in the area of HNP-based NLO microscopy have been reported. This includes the validation of imaging characteristics of HNPs [3,8] and of their

biocomapatibility [9], the linkage to interferometrically-based microscopy [10] and its successful applications for addressing research questions in nanobiophotonics [11,12]. Striking progress is reported in the chemical synthesis of novel types of polar ferroelectric HNPs as well (see e.g. [13–15] and references therein). This paves the way for multimodal HNPs, that combine nonlinear optical imaging with e.g. the local adjustment of a potential change via the photovoltaic effect, acoustic imaging via the acousto-optic or piezoelectric effect, or upconversion mechanisms by doping with rare earth elements. Despite these achievements, the potential of HNP-based NLO microscopy for deep tissue imaging is still controversially discussed – primarily because of a presumably low light yield of HNPs. In particular, applications in the field of nonlinear *in-vivo* imaging of HNPs and the respective simultaneous tracking have therefore not been studied so far because of a lack of an appropriate investigation tool enabling the possibility to image via nonlinear effect in a millimeter area with a sufficient signal to noise ratio.

To overcome this, we propose to change the way in which the required intensity is obtained, by increasing the energy per pulse in the μJ regime, instead of employing high repetition rate. This paves the way to expose a large sample area with sufficient intensity without focusing at all, i.e. a large field of view is achieved exceeding the area of any other widefield NLO system to the best of our knowledge. In particular we succeeded in *in-vivo* tracking of $KNbO_3$ harmonic nanoparticles with (i) a remarkable field of view up to $(1.5 \times 1.5)\,mm^2$, (ii) at a frame rate of 70 frames per second. Consequently the repetition rate is decreased in the kHz regime to keep the average power as low as possible in the mW regime. Technologically this is possible by using regeneratively amplified fs-pulse laser system. At the same time, the amplified pulses can be used to pump an optical parametric amplifier, so that the pump (and thereby the signal) wavelength can be adjusted for a spectral region of low tissue absorption. This technological combination make possible to create a Tunable hIGh EneRgy (TIGER) widefield microscope.

As social relevant application, and for system validation, *in-vivo* tracking of polar ferroelectric $KNbO_3$ HNPs is studied with the goal to access the blood circulation in the heart of a larve, a quantity linked to the study of cardiac disease. The Drosophila is in fact nowadays recognised as model for such type of studies [16]. For this, an illumination area in the millimeter regime is recommended to have a visual access to the complete heart chamber at once and frame rate in the millisecond regime are required to image with sufficient temporal resolution the flux [17]. The successful application of this approach is based on a profound knowledge of the nonlinear optical properties of the HNPs, the optical properties of the studied sample and the photometric properties of the used detector unit. In addition, to access the blood circulation, HNPs with diameters below 100 nm needed to be prepared. Our study therefore spans the HNP synthesis, the optical design and NLO characterization and the validation.

Our findings moreover demonstrate the large impact of the microscopic systems' flexibility in respect of repetition rate, energy per pulse and photon energy. Based on an iterative optimization procedure of the SNR, we finally elaborate a step-by-step-instruction for a more general use of *in-vivo* HNP-tracking, such as for widefield imaging at high frame rates with exceedingly high spatial and temporal precision mandatory for biological research questions.

2.   Experimental setup and material

2.1.   *$KNbO_3$ nanopowder synthesis*

$KNbO_3$ nanocrystals are used as harmonic nanoparticles throughout this study. The nanocrystals were prepared using a hydrothermal synthesis route as described in detail in [13]. In this case the ratio of Nb to KOH of 1 : 17 was used. As a result about 1.8 g $KNbO_3$ powder has been obtained as powder sample and was structurally validated by means of X-Ray diffractometry. A Panalytical Empyrean Diffractometer (Cu K_α radiation, BBHD-mirror, 0.04 rad soller slits, 1/2° anti scatter slits, 1/8° divergence slit, 2Θ step size: 0.026°) was applied. Rietveld (Fig. 1(a)) resulted in a mean crystallite size of about ~ 110 nm with the model of monoclinic $KNbO_3$ (space group

P1m1) [18]. Although also an, actually expected, orthorhombic phase (space group Amm2) can be well fitted, this gives slightly worse reliability factors than for the monoclinic phase (R_{exp} = 0.91%; R_{wp} = 2.75% orthorhombic ; R_{wp} = 2.53% monoclinic) [19]. No surfactants providing electrostatic or steric repulsion were used during the entire synthesis procedure. Thus, agglomeration of the crystallites in solution could not be prevented, as can be seen from the images using transmission electron microscope (TEM recorded with a EM-24830FLASH camera (JEOL) on a JEOL JEM-2100Plus (LaB_6 cathode, 200 kV)) in Fig. 1(b)).
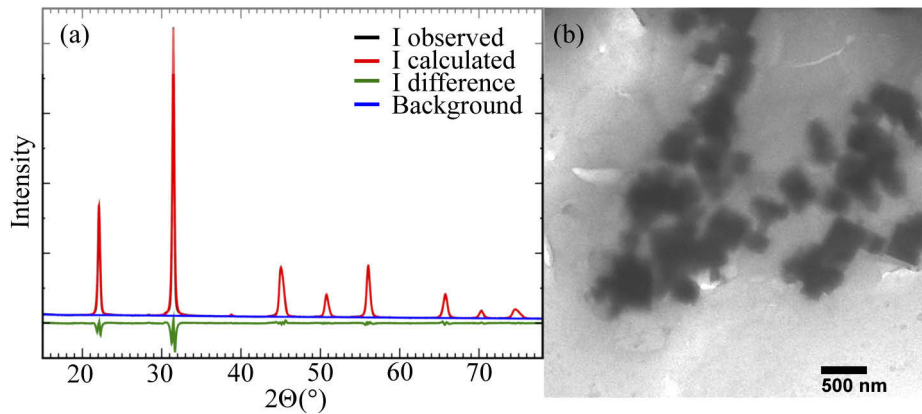

Fig. 1. (a) XRD with Rietveld analysis of the $KNbO_3$ powder sample. (b) TEM image of the powder sample. The redispersion with the use of tetramethylammonium hydroxide in methanol leads to a contamination of the TEM-grid which reduces the contrast. Agglomeration of the nanoparticles is clearly visible.

2.2. Preparation of microscopy slide

HNPs dissolved in ethanol were dropped onto a standard microscope cover slide, dried in air and at room temperature. A thin layer of HNP nanoparticles with a total area of 7 mm x 7 mm remained. Samples with the best homogeneity with respect to their particle distribution were used for the NLO studies. We note that the NPs adhered on the substrate without any further chemical support.

2.3. Preparation of larvae and transmission features

Drosophila melanogaster larvae were prepared as described previously [17]. In brief, for the performed measurements, only third instar larvae at the wandering stage were used. At this developmental stage, animals do not exhibit significant pigmentation (melanin, etc.) that, if present, could significantly contribute to one-photon absorption in the near-infrared range [20]. The body length at this developmental stage is 4 to 5 mm. Larvae were pinned with the dorsal side down onto plates filled with Sylgard 184 silicone elastomer. Specimens were covered with artificial hemolymph [21] which mimics the natural body fluid of *Drosophila melanogaster* larvae. The larvae were dissected from the ventral side and viscera (gut, trachea etc.) were carefully removed, avoiding any mechanical damage or stress on the linear heart tube. After a recovery time of approximately 5 minutes, the heart beats continuously for a couple of hours. For statistical purposes, experiments were performed within 30 minutes after preparation. A typical experiment starts immediately after the recovery period by adding a drop of $KNbO_3$ nanocrystals dissolved in artificial hemolymph. The drop (50 μl) was directly placed onto the dissected larvae above the heart. After delay period of one minute to allow the crystals to disperse, the plate was placed in the microscope for investigation.

Transmission characteristics were determined with a spectrometer via analysis of mechanically grinded larvae in order to assess an optimal wavelength window for HNP-excitation and detection as shown in Fig. 2.
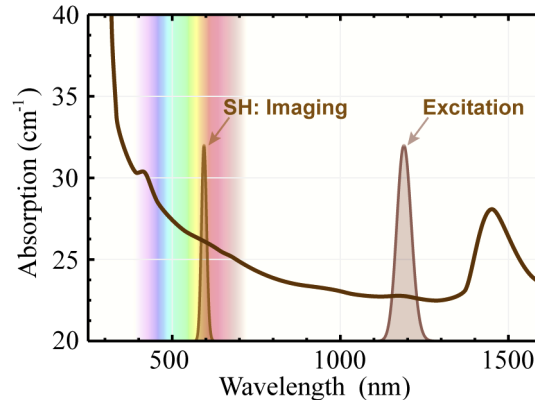

Fig. 2. Absorption spectrum of grinded *Drosophila melanogaster* larvae. The two peaks mark an exemplary wavelength configuration of fundamental (right) at 1190 nm and second harmonic (595 nm, left).

Throughout the investigated spectral region $\lambda = (250 - 1600)$ nm, the sample shows strong light attenuation with a minimal absorption coefficient $\alpha_{min} \approx 23$ cm^{-1} located in the infrared region around 1300 nm. For longer wavelengths towards 1450 nm, water absorption bands impair transmission [20], thus defining an upper limit for the excitation wavelength. In the opposite direction, the absorption rises monotonously producing a strong light suppression, so that wavelengths around 400 nm are the lower limit for imaging. For multi-harmonic detection, the ideal excitation/emission configuration is therefore to be chosen such that the fundamental spectrum is adjacent to the water absorption band, locating the second harmonic wave to the yellow-ed between $(550 - 670)$ nm spectral region. We like to add that investigations in the absence of HNPs reveal that (intact and living) *Drosophila melanogaster* larvae exhibit third harmonic generation upon irradiation with femtosecond pulses. At the same time, no intrinsic second harmonic generation has been observed. It is thus reasonable to focus our study on the detection of second harmonic emission by HNPs.

2.4. Optical setup for nonlinear imaging

Figure 3 shows a schematic sketch of the optical setup used in this work.

It consists of two major system parts: (1) a (confocal laser scanning) microscope, model: FV3000 (*OLYMPUS EUROPA SE & CO. KG*) that has been optically combined with (2) a regeneratively amplified high-power fs laser system, model: Pharos-HE-20 (*Light Conversion, Inc.*). The FV3000 is an inverted microscope and we here use two objectives with magnification: 4x (UPLANFL,Olympus) and a 10x (UPLANFI,Olympus), having a working distance of 17 and 10 mm and numerical aperture of 0.13 and 0.3 respectively. A filter cage in the optical path transmits the magnified image in the visible range onto a 2D CMOS sensor array while infrared light is reflected and blocked. Specifications of the Peltier-cooled camera system are: 16-bit grey scale sensor array, a maximum of 70 frames per second, at image resolution of 2048 x 2048 pixels, type: ORCA-Flash4.0 V3 Digital CMOS (Hamamatsu Photonics Deutschland GmbH). The sensor of the camera system is placed behind a fast filter wheel, that is equipped with a total of 8 interchangeable laser line filters in accordance with the choice of fundamental and harmonic wavelength pairs (blocking the residual of the fundamental and transmitting for the harmonic
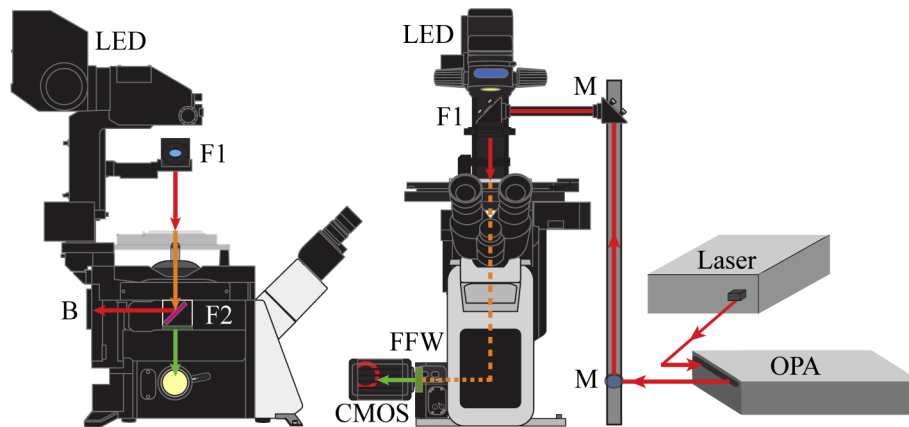
Fig. 3. Sketch of side (left part) and front view (right part) of the custom built nonlinear microscope. A regenerative amplified fs-laser acts as a source for an optical parametric amplifier (OPA) which in turn is coupled into an inverted microscope frame via a periscope. The light emitted by the sample is collected by an objective, filtered from the fundamental pulse radiation and redirected onto a CMOS camera. Legend: M: mirror; F: filter; B: blocker; FFW: fast filter wheel

light). The laser scanning unit, offering a total of five continuous-wave optically pumped semiconductor lasers, is not used in this study. Instead, a regenerative amplified diode-pumped Yb:KGd(WO$_4$)$_2$ (Yb:KGW) laser [22,23], serves as primary pump light source. The laser generates sub-ps laser pulses with typical pulse durations of ≈ 260 fs at a center wavelength of 1030 nm. A modified resonator design enables a maximum average output power of 20 W, i.e. of up to 400 μJ at a pulse repetition rate of 50 kHz. Several parameters of the pump laser can be tuned over a large range: the pulse duration can be stretched up to 10 ps; the pulse repetition rate can be increased from single pulse operation until 1 MHz and the pulse peak energy is adjustable from $1 - 400 \mu$J. As remarkable feature, the maximum pulse energy of 400 μJ is available for a large range of pulse repetition rates from single pulses up to 50 kHz. Still, 20 μJ are available at 1 MHz. This exceeds the pulse peak energies of high-power Ti^{3+}:Al$_2$O$_3$ oscillators by two order of magnitudes.

The laser acts as a pump source for a high power optical parametric amplifier (OPA), model: Orpheus F (Light Conversion). The fully automated, two-stage, non-collinear optical design enables the wavelength conversion in the range from 640 to 2630 nm. At the exit of the OPA, the pulses can be redirected to a pulse compressor, thus delivering pulses as short as ~60 fs, Alternatively, uncompressed pulses with ~180 fs can be used. Best performance of the OPA is obtained using a fixed pulse repetition rate of the pump of 50 kHz.

Coupling of the as-generated pulses into the microscopic system is realized using a two mirror (M) periscope to elevate the optical path up to the top of the microscope stage. The pulses are adjusted collinear to the optical path of the white light LED exchanging the condenser with a filter (F1), that reflects infrared light while visible light is transmitted. In this way the white LED light can also be used such that correlated linear and nonlinear optical images can be generated. Care is taken to suppress residual output of the OPA in the visible spectral range (e.g., the second harmonic of the pump light) by means of an appropriate longpass filter (LPF) along the beam path between the OPA and the periscope. In general, the optical path length between the OPA and the sample is reduced to a minimum in order to suppress any environmental influence on the pulse parameters (fluctuations of temperature, air flow, etc.) that give rise to unwanted phenomena such as pulse broadening. For the purpose of applications in optogenetics the installation is embedded

in an environment of biological safety standard S2 . This does not only ensure a high standard with respect to biological functionality; it also offers working places for chemistry preparation in direct vicinity of the optical setup.

The detailed characterization of the energy per pulse in function of the wavelength and repetition rate calculated at the sample position in the microscope are reported in Fig. 4.
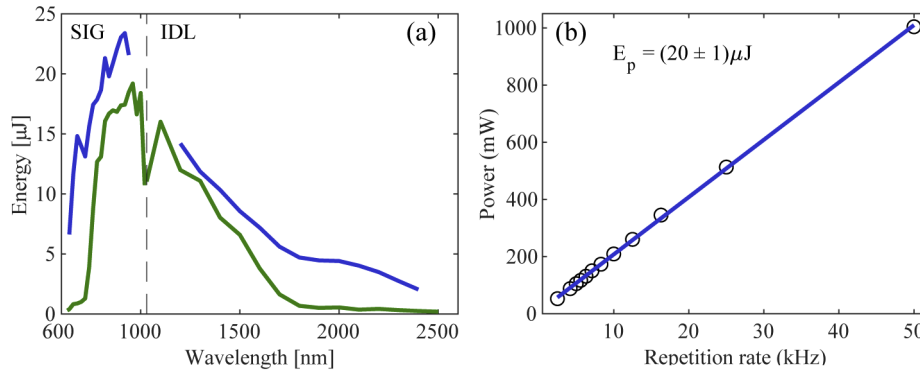

Fig. 4. (a) Energy per pulse measured at the microscope sample position in function of the central wavelength of the OPA spectra for uncompressed (green curve) and compressed (blue curve) pulses at a repetition rate of 50 kHz. The vertical dotted line separates the wavelength range of the signal (SIG) and the idler (IDL). (b) Time-averaged power as a function of repetition rate for the wavelength of 964 nm uncompressed (black data points). A linear fit (blue line) has ben fitted to the experimental data and yields an energy per pulse of $E_p = (20 \pm 1)\,\mu J$.

The energy per pulse in Fig. 4(a)) is calculated from the average power determined at the maximum repetition rate. Pulse energies between 1 and 24 μJ are obtained in the spectral region from 600 to 1800 nm with a maximum of $(24\pm1)\,\mu J$ at about 900 nm for the compressed signal. The average power in function of the repetition rate of Fig. 4(b)), measured for the exemplary wavelength of 964 nm uncompressed, shows that the energy per pulse is constant over the available repetition rate regime (1 - 50 kHz). In particular, a linear fit of the data reveals an average pulse energy $E_p = (20 \pm 1)\,\mu J$.

2.5. Imaging analysis

Video and images are acquired via the Olympus software CellSens. Several parameters can be adjusted during the experiment as the exposure time (from 10 ms till 1 s), the LED brightness and the number of pixel per frame, which in our case is always fix at 2048 x 2048. The resulting video (see Visualization 1) is cropped to select only the heart structure via Fiji software. This one is also used for the nanoparticle tracking analysis via the plugin "Manual tracking". The latter one requires the information on the pixel calibration and the time between two frames. This allows for the extraction of the particle position in each frame and, consequently, of the particle distance and the speed compared to the previous frame. This information is then processed with Matlab to create the vector plot. It is done in a straightforward manner via the *quiver* plot which only requires the knowledge on the particle position as well as on the vector speed projection in a XY system.

3. Experimental results

3.1. NLO characterization of KNbO₃ nanoparticle powder

Figure 5 shows the experimentally determined intensity of $KNbO_3$ nanoparticle harmonic emission powder using the nonlinear diffuse fs-pulse reflectometry technique described in Ref. [24,25]. Briefly, the sample is prepared pressing a powder pellet, the laser source (cf. section 2.4) is loosely focused into the sample with the focus point being behind the sample. Intensity modulation is achieved by means of a variable neutral density filter wheel. Diffusely backscattered harmonic radiation is then filtered via a short pass filter and collected perpendicular to the surface of the sample using a spectrometer (QE *Pro*, Ocean Optics). Figure 5(a)) shows the harmonic emission at a center wavelength of 482 nm (blue data points) as a function of the pump average power of the fundamental light (center wavelength $\lambda_{p0} = 964$ nm, PRR: 50 KHz) in a double-logarithmic plot. A power function of the type $I_{SHG} = m \cdot I_p^n + b$ has been fitted to the experimental data (blue line) and yields an exponent of $n = (2.0 \pm 0.2)$ in the power range up to a maximum value of $P_p = 350$ mW. A deviation of the fitting function from the data points exceeding the experimental error is clearly observed at maximum pump intensities. This behavior is most probably ascribed to the depletion of the SH signal, which can be used as an intermediate field to generate third harmonic emission [26]. Figure 5(b)) shows the spectral dependence of the $KNbO_3$ powder harmonic emission in the wavelength range from 460 - 550 nm and for different repetition rates from 1-25 kHz. The same wavelength pair ($\lambda_{SHG} \approx 482$ nm; $\lambda_{p0} = 964$ nm) was used at a pump intensity of $I_p = 1 \cdot 10^{15}$ W/m² for all spectra. A clear decrease of the SH signal for decreasing PRR is observed, while the spectral shape of all measurements do not change.

Figure 5(c)) shows the nonlinear emission spectra as a function of the pump light center wavelength from 850 nm $< \lambda_{p0} <$ 1400 nm at a repetition rate of 50 KHz in a colour plot. According to the output characteristics of the OPA, the pump intensities of the individual measurements varied from $1.9 \cdot 10^{14}$ W/m² up to $8.7 \cdot 10^{14}$ W/m², so that the spectra have been normalized to their respective maxima. The plot shows the linear wavelength relation between harmonic and fundamental light. In addition, the appearance of (weak) third harmonic generation (THG) is observed in particular in the wavelength range from 1050-1250 nm (here, the OPA output features its maximum pulse peak energy). Plots of the functions $\lambda_{SHG} = 1/2 \cdot \lambda_{pump}$ and $\lambda_{THG} = 1/3 \cdot \lambda_{pump}$ are added to the color plot (straight white line). A clear accordance with the peak wavelengths of all spectra is found.

3.2. NLO imaging of KNbO₃ nanoparticle layers

Figure 6 shows the results for NLO imaging of $KNbO_3$ nanoparticle layers prepared on a microscopy cover slide (cf. section 2.2) using the NLO microscopic setup described in chapter 2.4 with a 4x magnification objective in a)-c) and a 10x one in d)-f), respectively. The images of SHG emission at ≈ 482 nm in parts b) and e) were obtained during exposure with the pump laser at $\lambda_p = 964$ nm (PRR=50 kHz) and in transmission geometry. A moderate pulse peak intensity of $5 \cdot 10^{13}$ W/m² was chosen in order to avoid thermooptical damages to the sample. For comparison, parts a) and d) show the same sample using the LED lamp and both images were superimposed as correlated images in parts c) and f).

A filter of type 482/25 (narrow bandwidth transmission filter with center wavelength of 482 nm and bandwidth of 25 nm) was placed in front of the CMOS sensor array in order to adapt the spectral detection window with the SHG emission band, i.e. fundamental and THG light as well as any other undesired stray light source have been suppressed by up to five orders of magnitudes. Images were acquired for durations of 1.3 s in Fig. 6(b)) and 910 ms in Fig. 6(e)), corresponding to a train of 65000 and 45500 pulses, respectively.

We note that exposure was realized using the unexpanded laser pulse train as reflected from the OPA via the photon trap onto the sample, i.e. in a NLO widefield imaging mode. An average
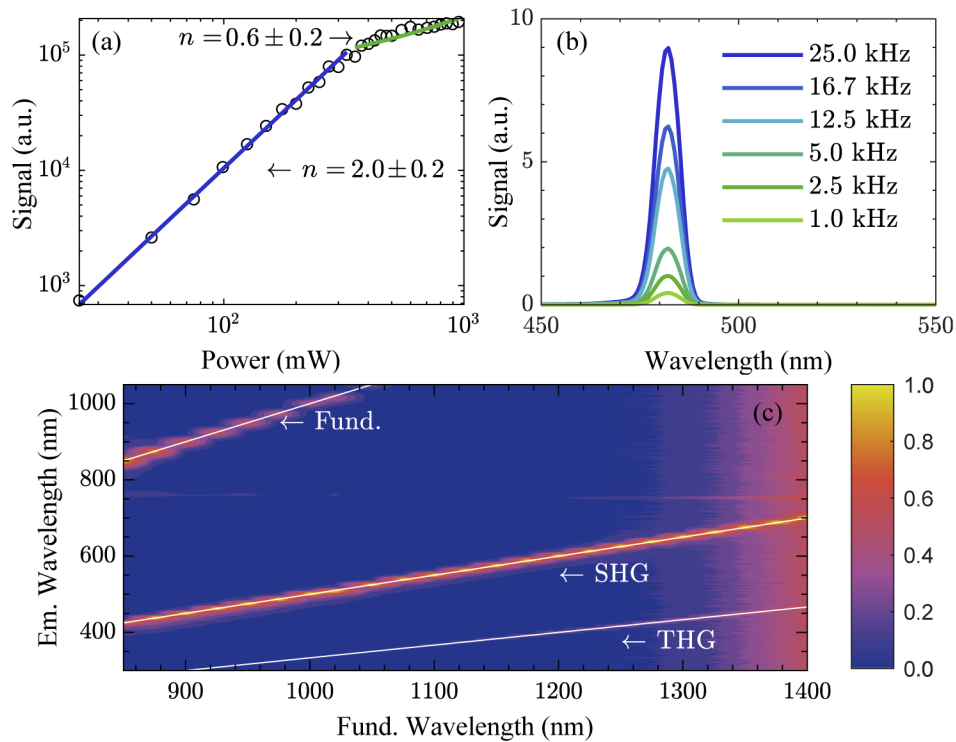
Fig. 5. (a) SHG signal at 482 nm (blue data points) as a function of the pump average power of the fundamental light (λ_{p0} = 964 nm, PRR: 50 KHz) in a double-logarithmic plot. A power function has been fitted to the experimental data (red line) and yields an exponent of $n = (2 \pm 0.1)$ in the power range up to $P_p = 2.5 \cdot 10^2$ mW. (b) Spectral dependence of the harmonic emission of the $KNbO_3$ powder in the wavelength range from 450 - 550 nm and for different repetition rates from 1-25 kHz. The same wavelength pair ($\lambda_{SHG} \approx 482$ nm; $\lambda_{p0} = 964$ nm) was used for all spectra. (c) Normalized SHG spectra as a function of the center wavelength of the pump light from 850 nm$<\lambda_{p0}<$1400 nm at a PRR of 50 KHz in a colour plot.

beam diameter of $(2076 \pm 30)\,\mu m$ ($1/e^2$-value, $\lambda = 964$ nm) at the position of the image plane was determined. Together with the energy per pulse (see Fig. 4(a)), an upper limit of the energy density of about $0.6\,mJ/cm^2$ can be estimated for the pulses of our studies and setup at the imaging plane of the biological sample. This energy density is much below the damage threshold value for the interaction of short laser pulses and biological tissue ($100\,mJ/cm^2$) as published by the statutory accident insurance (GUV-V B2) [27]. Using the 4x objective in Fig. 6(a))-c), the entire area of SHG emission could be successfully acquired. From image analysis, an effective area, i.e. the area where considerable SHG emission can be generated, of about $(1500 \times 1500)\,\mu m^2$ ($1/e^2$-value, $\lambda = 482$ nm) has been verified. Figures 6(d))-f) demonstrate that a mostly spatial homogeneous SHG is obtained using a 10x objective that may be advantageous for particular SHG imaging studies. In the next step, the signal-to-noise-ratio (SNR) of each image has been determined and served as key measure for further inspection of the NLO imaging features. We here use the most common definition of the SNR, being the ratio of the average intensity of the signal over the standard deviation of the noise. Therefore, it can be deduced by the histograms plot of the images, as exemplarily depicted for image Fig. 6(e)) in Fig. 7(a)) in a double-logarithmic plot. Two main features are observed. The peak at low grey levels between $(1 - 10) \cdot 10^2$ correspond with the dark background pixels of the image, i.e. to the parts of the
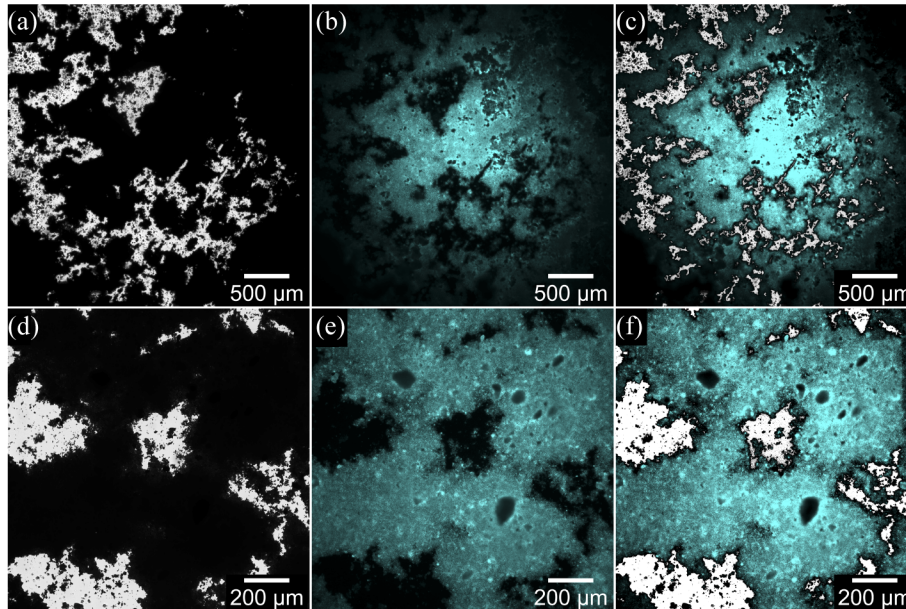
Fig. 6. (a) Bright field image of a KNbO$_3$ layer acquired using the LED lamp as light source with a 4x objective. (b) SHG emitted at $\lambda = 482$ nm by the same layer presented in (a) when exposed to $\lambda = 964$ nm, $\nu = 50$ kHz and acquired with 1.3 sec of camera exposure time. Image is presented in pseudocolor. (c) SHG image superimposed to the bright field image. (d) Bright field image of a KNbO$_3$ layer acquired using the LED lamp as light source with 10x objective. (e) SHG emitted at $\lambda = 482$ nm by the same layer presented in (d) when exposed to a laser at $\lambda = 964$ nm, $\nu = 50$ kHz and acquired with 910 ms of exposure time of the camera. Figure is presented in pseudocolor. (f) SHG image superimposed to the bright field image.

microscope cover slide that do not contain nanoparticles. The respective peak can be fitted with a Gaussian distribution and reveals its maximum at $(5.3 \pm 0.1) \cdot 10^2$ and a standard deviation of the image dark noise of $(3.1 \pm 0.2) \cdot 10^2$. In contrast, the feature with a maximum at higher gray levels (peak maximum at $(6.9 \pm 0.3) \cdot 10^3$) accords with the intensity of SHG emission.

According to this image processing procedure, the SNR was determined as a function of incident pulse energy as shown in Fig. 7(b)). Again, the KNbO$_3$ layer used for the imaging in Fig. 6, a PRR of 50 KHz, and a laser wavelength of 964 nm were used. The camera system, equipped with the filter 482/25, is set to a fixed exposure time of 1000 ms. The energy per pulse is modulated by changing the average power via neutral density filters in the range from $10^{-7} - 10^{-5}$ J, i.e. over three orders of magnitude. As a result, the SNR can be doubled up to a value of ≈ 75. However, a peak value is reached at a pulse energy of $E_p = 8 \cdot 10^{-6}$ μJ such that the SNR decreases for a further increase of E_p.

The result of the study of the SNR as a function of the repetition rate is given in Fig. 7(c)). This is done at the same sample spot and with the same parameters used for the analysis in function of the energy per pulse. Here the difference is that the repetition rate is modulated via the laser software while the pulse energy remains constant at a value of $E_p = 20$ μJ. As it can be seen the SNR remains constant as a function of the repetition rate. We like to note, however, that the dynamic range of the camera decreases with decreasing repetition rate.

In Fig. 7(d)) the dependence of the SNR in function of the wavelength is studied. This dependence is the complex result of SHG efficiency generated by the NP, the laser intensity
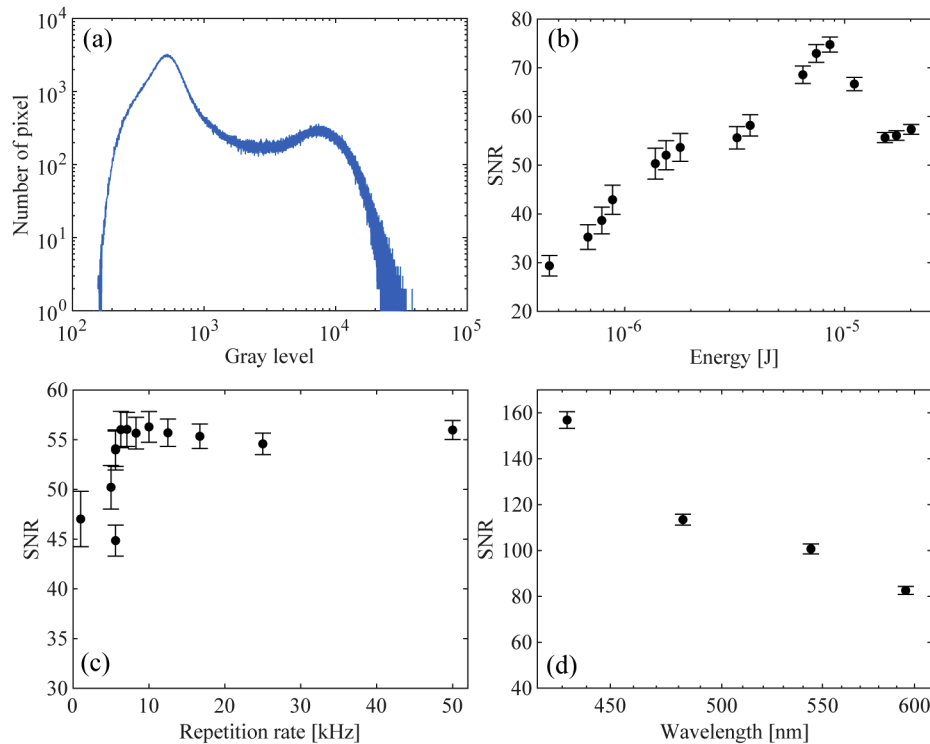
Fig. 7. (a) Example of an image histogram acquired with same parameters of Fig. 6(e). (b) Signal to noise ratio as a function of the energy per pulse. (c) Signal to noise ratio as a function of the laser repetition rate. (d) Signal to noise ratio as a function of the emitted wavelength.

dependence as a function of the wavelength (Fig. 4(a)), the camera efficiency, which has a maximum around 550 nm and all the optics that are inside the microscope, as the objective.

3.3. *System validation: in-vivo tracking of HNPs in Drosophila melanogaster*

The harmonic widefield microscope described and characterized in previous sections is suitable to perform real time studies where the dynamic exploits SHG in a millimeter area and in the millisecond time regime. For validation of this functionality, we study the hemolymph flux of *Drosophila melanogaster* larvae system by tracking HNPs perfused in the heart chamber. This flux is expected to be in the range of μm/ms [17], therefore single frames captured with an exposure time in the millisecond range are necessary to analyse the dynamics at a sufficient temporal resolution. In addition, an illumination area in the millimeter regime is recommended to image the complete heart chamber at once. This is an appealing approach to gain new insight because the single-particle tracking methods can provide local information usually not accessible [28].

Based on result of Fig. 2, a fundamental wavelength at 1190 nm is chosen, close to the water absorption band, locating the SHG at 595 nm. Despite of the lower sample absorption in the IR, attention has to be paid to the cellular photodamage, due to the high peak intensity of the laser pulses. In this respect the thermal energy deposited by a single pulse may be negligible, but the cumulative effect of several pulses may easily induce damage; in this case the time between pulses (i.e. the laser repetition rate) also needs to be considered, with lower values reducing the thermal stress/strain on the sample. For this purpose, a repetition of 5 kHz (a pulse every

0.2 ms) is found to be a good value because using these settings, necrotic (brown or black) spots were not observed in the animal's tissue after laser exposure. The camera exposure time was set to 10 ms, resulting in 50 light pulses per image. Before applying HNP to animal tissue, we tested the chosen setting on HNP in solution. The widefield image using LED illumination is shown in Fig. 8(a)), the corresponding SHG image is depicted in Fig. 8(b)) while Fig. 8(c)) is the superposition of (a) and (b). We found that under these conditions enough signal can be collected to distinguish it from background. The signal to noise ratio (SNR) is 27.
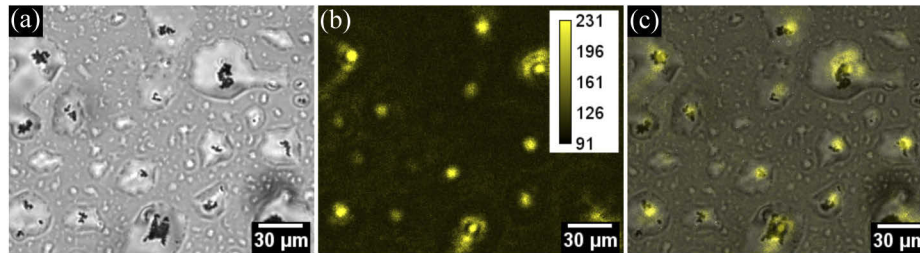

Fig. 8. (a) Bright field image of small microcluster and (b) SHG from the same microclusters exposed at 1190 nm, 5 KHz. The objective is a 10x magnification and camera integration time is 10 ms. Image is presented in pseudo-color (c) SHG image superimposed with the bright field image. Please note that the sample was not completely dried to validate the NLO functionality of the HNPs in a fluidic environment.

Figure 9 gives an overview of the dissected *Drosophila melanogaster* larva used for our study and prepared according to the procedure described in section 2.3. The bright-field images of Figs. 9(a)), b) clearly show the heart system with trachea, posterior heart chamber, anterior aorta
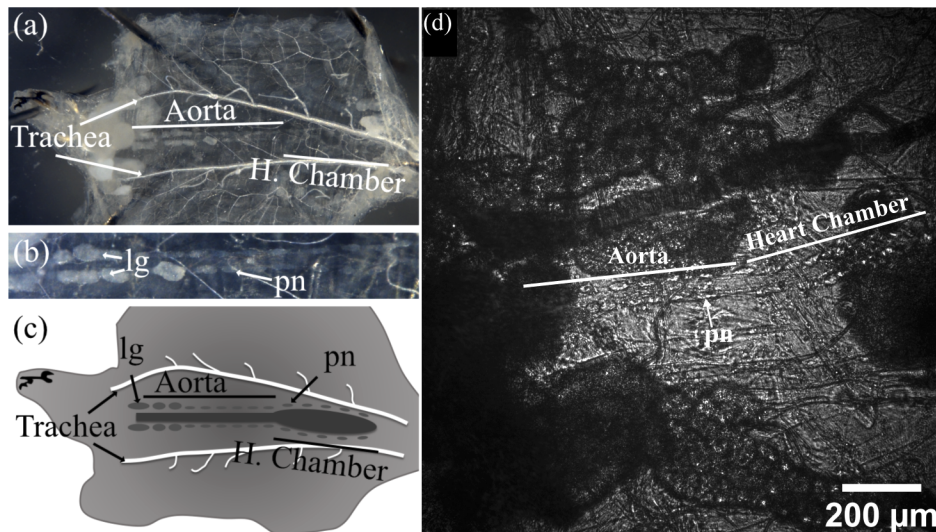

Fig. 9. (a) Bright field image of a dissected *Drosophila melanogaster* 3rd instar larva. The dorsally located heart is flanked by prominent trachea and consists of a posterior heart chamber and an anterior aorta region. (b) Enlargement of the aorta region with lymph glands (lg) and pericardial nephrocytes (pn) located laterally to the heart tube. (c) Schematic illustration of a dissected 3rd instar larva showing heart tube divided into aorta and heart chamber. (d) Example of one frame extracted from the recorded video showing the dissected *Drosophila* 3rd instar larva heart laterally flanked by pericardial nephrocytes (pn).

region, lymph glands (lg) and pericardial nephrocytes (pn) along the heart tube (see also sketch in Fig. 9(c))). The same parts of the larva are visible in the SHG-image shown in Fig. 9(d)), that was captured in our setup under exposure to laser light and after dispersion of the HNP particles within the hemolymph. This figure was extracted from one of the recorded videos (analysed below in more detail) and exhibits a larger contrast and grey scaling in direct comparison with the bright field image. It is due to the bandwidth filter centered at 595 nm and inserted into the fast filter wheel that enables the spectrally sharp detection of the SHG signal emission. At the same time, residual background light, resulting from the transmitted fundamental laser light, becomes strongly suppressed by the filter.

From the inspection of Fig. 9 we can further conclude, that some particles aggregate and stick to tissue. These immobile clusters cannot be used for HNP tracking with the hemolymph, but turn out to be very valuable for the simultaneous imaging of the dynamics of the heart system itself. Many HNPs were sucked into the heart chamber and circulate together with the hemolymph. Upon continuous heart beating activity, these HNPs flow with the hemolymph through the heart tube from posterior heart chamber to the anterior aorta region of the heart tube. The obtained video shows both, the beating heart and the movement of individual HNPs within the heart tube, and can be seen in the Supplementary material.

In the next step, the video data was applied for HNP tracking and the validation of an experimental access to the streaming properties inside the heart system, as depicted in Fig. 10. For this purpose, the position of individual HNPs were marked in a series of subsequent images, as shown in Fig. 10(a)). Then, the HNP track was reconstructed from the comparison of the NP positions in subsequent frames (Fig. 10(b)) at a mutual time delay between two images of 14 ms. Using the scale of the microscope, the frame rate and the determined distance, we were able to
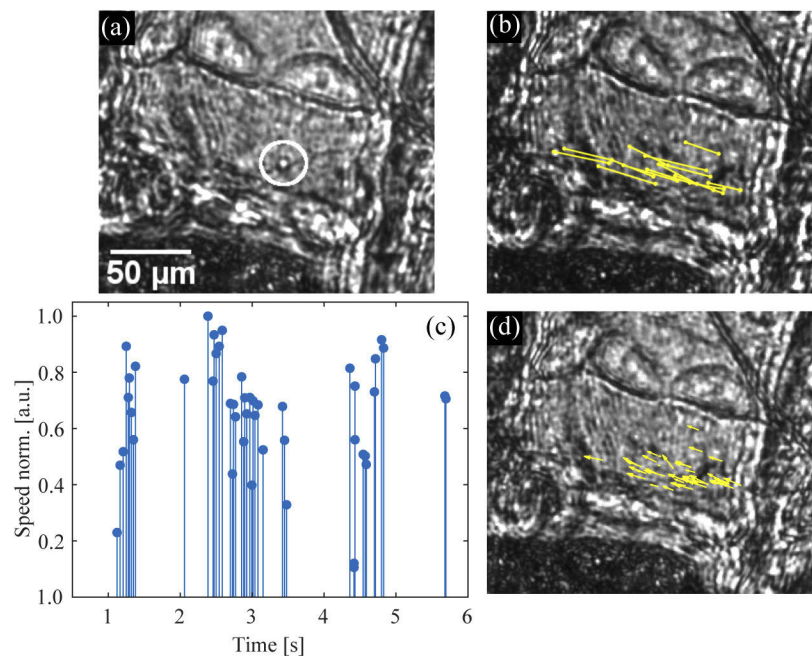

Fig. 10. (a) Zoom of Fig. 9(d) where an HNP flowing in the heart chamber is visible in the white circle. (b) Result of the tracking procedure where in yellow the trajectory of some nanoparticles are depicted (c) Normalised speed of the tracked HNPs as a function of time. (d) Vector plot correlating the speed information of (c) with the spatial analysis obtained in (b).

determine the individual velocity of a large number of HNPs with which the respective statistical distribution depicted in Fig. 10(c)) was deduced as a function of time of the video. Note, that the lack of data at times of about 2 and 4 seconds relate with the disappearance of the SHG signal and/or a lack of particles, as will be discussed below. In the final step, the velocity data were transferred into vectorial data by additional consideration of the HNP track direction and the vectorial map of Fig. 10(d)) is obtained by correlation with the first frame of the video.

4. Discussion

Our study reveals *in-vivo* access to the streaming properties inside the heart tube of a living organism using polar ferroelectric HNPs as nanoscopic light sources. The images and videos unambiguously demonstrate the generation of a sufficient light yield at 70 frames per second using a regeneratively amplified fs-laser system. This equals access to a hemolymph flux of 10000 μm/ms. Our approach represents a valuable step forward for enabling systematic studies based on *in-vivo* tracking and comprises a sound potential to foster further understanding of flow properties and their relation with the intraluminal structure.

4.1. Step-by-step instruction

According to the success of our stepwise procedure, we are able to deduce the following, generalized step-by-step instruction for HNP tracking in living organisms: as reliable starting point (Step 1) serves the very basic physical relationship between pulse peak intensity I_{p0}, pulse energy E_p, average power P_{avg}, pulse duration τ_p, pulse repetition rate PRR and area of illumination A for the design of the experiment:

$$I_{p0}(\lambda) \simeq \frac{E_p(\lambda)}{\tau_p(\lambda) \cdot A} = \frac{P_{avg}(\lambda)}{\tau_p(\lambda) \cdot A \cdot PRR} \quad . \tag{1}$$

This equation primarily enables the optimization of the second harmonic conversion efficiency, which scales with the square of I_{p0}, by a proper selection of pulse parameters and, thereby, of the laser system itself. The impact of the individual parameters of Eq. (1) can be evaluated as follows: the illumination area A determines the maximum pulse peak energy of the laser system. The repetition rate *PRR* and pulse duration $\tau_p(\lambda)$ are the driving parameters to limit the time-averaged power P_{avg} with respect to the (thermo-optical) tissue damage. The latter can be reduced by changing the wavelength of the incident pulse such that minimal light absorption is attained in the sample under investigation (cf. Figure 2). However, the dispersion of the output pulse energy of the OPA should be kept in mind (see Fig. 4). As a rule of thumb, decreasing the pulse duration will increase the conversion efficiency, while decreasing the PRR values will increase the damage threshold [29]. In our case, the average power of the fundamental was inspected as a function of the PRR up to 50 kHz, showing a linear increase with a maximum value of about 1 W as shown in Fig. 4(b)), i.e. small PRR values will be strongly recommended. We also measured the SHG signal as a function of PRR in Fig. 5(b)) that, in contrast, requires PRR values as large as possible in the view of a large SNR. Thus it is necessary to counterbalance SNR with the thermo-optical damage, which are specific for the system under study (they depend on the NLO features of the used harmonic nanoparticle and on the thermo-optical stability of the organism, respectively). In general, values in the kHz regime seem to be a good choice [30], but a detailed analysis is required for optimum adjustment. It is noteworthy that the approach of reducing the pulse duration for an increase of the SNR is connected in a similar way with a limitation. In particular, reaching a threshold pulse peak intensity I_{p0} may enable tissue damage mechanisms of the sample due to dielectric breakdown and/or polar pigmentation (melanin, etc.). Taking all these considerations of step 1 into account, a striking impact of the dependence of the nonlinear optical properties of the HNPs on the laser pulse parameters according to section (3.1) is emphasized.

The second step (Step 2) is to optimize the emission wavelength of the second harmonic emission to the absorption features of the sample and/or optical setup as well as to the spectral sensitivity of the detector. Here it is mandatory to secure that the SHG emission wavelength does not fall in the spectral region of the optical system band edge and/or of a pronounced absorption feature of the sample itself. This step thus requires the knowledge about the transmission features of the sample and of the optical system - this may be challenging by itself. Ideally, the emission wavelength shall coincide with the maximum of the spectral sensitivity of the detector. However, in most cases, this contradicts with the optimization results of step 1 as for the case of our study: the range of 1200 – 1300 nm could be chosen for the pump wavelength according to the transmission spectrum of Fig. 2 and, in particular, with a priority to longer wavelengths. This wavelength region is also in line with the remarkable dispersion properties of the $KNbO_3$ nanoparticles SHG emission depicted in Fig. 5(c)), that show efficient conversion between 850 and 1400 nm without any gap. Moreover, the emission wavelengths corresponding to this range of pump wavelengths are between 600 and 650 nm, and perfectly match with the sensitivity of the CMOS 2D detector in the visible spectral range with values exceeding 40% between 400 and 800 nm. On the contrary, a closer look to Fig. 4(a)) shows that any choice of pump wavelengths longer than 900 nm has in general a negative influence on the pulse energy and particularly decreases by about 50% from 1200 to 1300 nm. It is therefore necessary to iteratively repeat steps 1 and 2, so that the emission wavelength becomes as close as possible to the maximum value of the spectral sensitivity. One possibility to achieve this could be to increase the PRR according to the results shown in Figs. 5(a) and 5(b). In this sense, it is recommended to use the signal-to-noise ratio as control parameter during optimization of the iteration procedure. Taking these considerations, and the spectral features of the transmission filters of the microscopic systems into account, we ended up with pump wavelengths of 964 nm and 1190 nm for HNP imaging without and with the larvae (Fig. 6) and for the tracking experiments inside the *Drosophila* heart system (Figs. 8 and 9), respectively.

Step 3 is finally to optimize the SNR by fine tuning of the pulse energy and the integration time of the detector. According to our findings in Fig. 7(b)), the SNR features a maximum as a function of pulse peak energy that can be used for tuning. Again, an iterative optimization procedure with steps 1 and 2 becomes necessary since the SNR further is dependent on both, the PRR and the wavelength of harmonic emission. In particular, and according to our findings of Fig. 7(c)), the PRR should not be chosen much below 10 kHz, which appears to be contradicting with the aspect of thermo-optical damage, as discussed before. However, the SNR loss is comparably small with values between 45 (<10 kHz) and 55 (>10 kHz). By far more important is the spectral dependence of the SNR as depicted in Fig. 7(d)) that clearly points in favour of smaller wavelengths. An increase by a factor of ≈ 1.8 is found in the range between 400 (SNR = 85) and 600 nm (SNR = 155) that has a considerable impact on the tracking results. In addition, the possibility to tune the integration time of the CMOS 2D detector may be used. Here we note that increasing the signal by increasing the detector's integration time may result in an increase of the dark noise of the detector. In this case, cooling of the camera system is recommended, if not already installed.

So far, the previous considerations hold for a given HNP size distribution. In order to tune the conversion efficiency by the HNP itself and as alternatively to step 1, it is possible to tailor the HNP particle size. Assuming spherical particles, the signal intensity scales with the particle radius with the power of six [31]. The choice of particles with larger diameter therefore could be an interesting route. However, as it can be seen in our experiments as well, the HNPs then might stick to the tissue to a larger extent and will not be dispersed within the hemolymph. The cellular structure therefore defines the maximum allowed particle size and may even act as a filter if HNPs with large size distributions are used.

Choosing other polar ferroelectric crystals for the synthesis of HNPs to exploit their different nonlinear optical coefficients ($MNbO_3$ with M=K, Na, Li,. . . . or other ferroelectric perovskites like $LiTaO_3$ or $BaTiO_3$, etc.) might be a further approach to increase the conversion efficiency. These parameters do vary by a factor of up to 10. However, as most of the values are determined from bulky single crystals, the situation may be different according to size effects and/or morphology. For instance, it was shown only recently that sodium niobate nanocrystals generate second harmonic emission comparable to potassium niobate, though their respective bulk representatives differ by a factor of three to four [15].

In addition, the imaging quality not only depends on the SNR, but also on the homogeneity of the exposure. For nonlinear optical microscopy, the nonlinear dependence between incident pump pulse and signal yield amplifies any inhomogeneity in the intensity distribution of the incident pulse. Thus it is very important to carefully consider the required homogeneity in the final image. In our case, the homogeneity was obtained by a large over-exposure of the inspected area. The Gaussian profile was used within the region of maximum intensity, only. It means that a large loss of pulse energy was taken into account, i.e. the laser system needs to be over-dimensioned in this case. Today, there are not many fs-pulse laser systems, that deliver pulse peak energies in the order of $\approx 400\mu$J, but a further technology increase of commercial systems is to be expected in the laser market in the next years.

4.2. Access to streaming properties

We finally discuss the obtained tracking results in the light of inspecting the streaming properties in the heart tube of a *Drosophila* larva. A striking characteristic of the HNPs in the videos (see Supplementary material) is their short-time appearance, i.e. the SHG emission intensity is fluctuating as a function of time and space. However, this issue must not be mixed-up with the blinking and/or bleaching phenomena that are well-known for fluorescent dyes or quantum dots [1]. Instead, it is due to the polar structure of the HNPs that gives rise to linear polarized light emission within a plane being parallel to the polar axis [32]. As this axis rotates during the flow with the hemolymph through the heart tube, the direction of light polarization of the emitted signal changes as a function of time and space. We note that this feature does not appear in the study of HNP powder samples in subsection 3.1 due to an integrated signal emission from a large number of nanoparticles with a statistical mixture of the direction of the polar axis. Nevertheless, position and track of individual HNPs could be determined with sufficient precision and path lengths throughout the video sequences.

Another unexpected issue of our data is the different dispersion of the HNPs either forming immobile clusters that remain fixed in the heart chamber and individual HNPs flowing with the hemolymph. It turns out that both types of HNP are very useful for the purpose of streaming analysis, as HNP tracking can be directly related to the dynamics of the organism itself. This advantage therefore is particular significant for the study of *living* organisms. In our case, the additional information from the immobile clusters was very useful to verify the heart beat of the dissected larva.

As main result of the HNP tracking procedure, the statistical distribution of velocities over time and the velocity vector map shown in Figs. 10(c)), d) were deduced. The distribution highlights the large differences in the velocities of the HNPs at different positions at the same time within the heart system that deviate by a factor of up to ten. This result underlines the possibility to distinguish HNP velocities with sufficient precision. Remarkably, the distribution does not change as a function of time that additionally supports the reproducibility of the data set and the continuity of the flowing HNPs. Furthermore, it shows the sustained heart functionality, i.e. we can neglect a major influence of the HNPs and fs-laser excitation on the organisms at least over the period of time of inspection. It is therefore quite reasonable to assume that the determined HNP velocity resembles the flow velocity of the hemolyph to a large extent. This simplifies

the interpretation of the determined vector map in the framework of a deeper understanding of heart diseases. In particular, if the vector map is correlated with the image of the organism, as shown in Fig. 10 d) for instance, heart regions with too low streaming velocities can be extracted directly. The same holds for regions showing unwanted vortices and/or turbulences. Vice versa, the regions showing a laminar flow become accessible and their potential role for a healthy heart system can be studied.

5. Conclusion

Tracking of harmonic nanoparticles can be realized even inside living organisms by a proper design of a nonlinear optical widefield microscope, in particular by using a regeneratively amplified fs-oscillator with an optical parametric amplifier as pump laser source. The main focus lies on an extended range of parameters for optimization of the signal-to-noise ratio and includes not only the pulse parameters of the laser itself (photon energy, repetition rate, pulse energy), but also the dispersion features of the HNPs, of the camera and of the organism under study. In comparison with commercial multi-photon microscopes, the increased pulse energy is very much decisive for the success of the experiments demonstrated here, mainly because of two reasons: (1) it enables the optimization of the SNR such that HNPs can be tracked even at lowest image recording times of a few milliseconds, i.e., at large frame rates and (2) it allows for a quasi-homogeneous exposure of the field of view even at dimensions of a few hundreds of micrometers. Both aspects open up the determination of a statistical distribution of HNP velocities and of a velocity vector map with sound precision and reproducibility, that resembles a new type of access for the study of heart diseases. A large number of biological research questions can now be addressed, e.g., whether laminar flow properties apply and which intraluminal structures of the heart tube may cause turbulences. However, we also do expect that future studies will allow us to inspect living animals, as well, but also numerous other biological research question that requires far-field imaging at high frame rates with exceedingly high spatial and temporal precision. The prerequisite of a carefully tailored experimental setup can be deduced along the step-by-step instruction presented here.

Disclosures. The authors declare no conflicts of interest.

Data availability. Data underlying the results presented in this paper are not publicly available at this time but may be obtained from the authors upon reasonable request.

References

1. L. Bonacina, "Nonlinear nanomedecine: Harmonic nanoparticles toward targeted diagnosis and therapy," Mol. Pharmaceutics **10**(3), 783–792 (2013).
2. F. Helmchen and W. Denk, "Deep tissue two-photon microscopy," Nat. Methods **2**(12), 932–940 (2005).
3. C.-L. Hsieh, R. Grange, Y. Pu, and D. Psaltis, "Barium titanate nanoparticles used as second harmonic radiation imaging probes for cell imaging," in *Advanced Microscopy Techniques*, P. J. Campagnola, E. H. K. Stelzer, and G. von Bally, eds. (SPIE, 2009).
4. H. Zhao, R. Cisek, A. Karunendiran, D. Tokarz, B. A. Stewart, and V. Barzda, "Live imaging of contracting muscles with wide-field second harmonic generation microscopy using a high power laser," Biomed. Opt. Express **10**(10), 5130 (2019).
5. E. M. Rodríguez, A. Speghini, F. Piccinelli, L. Nodari, M. Bettinelli, D. Jaque, and J. G. Solé, "Multicolour second harmonic generation by strontium barium niobate nanoparticles," J. Phys. D: Appl. Phys. **42**(10), 102003 (2009).
6. D. A. Fernandes and M. C. Kolios, "Near-infrared absorbing nanoemulsions as nonlinear ultrasound contrast agents for cancer theranostics," J. Mol. Liq. **287**, 110848 (2019).
7. D. A. Fernandes, S. Appak-Baskoy, E. Berndl, and M. C. Kolios, "Laser activatable perfluorocarbon bubbles for imaging and therapy through enhanced absorption from coupled silica coated gold nanoparticles," RSC Adv. **11**(9), 4906–4920 (2021).
8. R. Grange, T. Lanvin, C.-L. Hsieh, Y. Pu, and D. Psaltis, "Imaging with second-harmonic radiation probes in living tissue," Biomed. Opt. Express **2**(9), 2532 (2011).

9. D. Staedler, T. Magouroux, R. Hadji, C. Jouland, J. Extermann, S. Schwung, S. Passemard, C. Kasparian, G. Clark, M. Germann, R. Le Dantec, Y. Mugnier, D. Rytz, D. Ciepielewski, C. Galez, S Gerber-Lemaire, L. Juillerate-Jeanneret, L. Bonacina, and J. -P. Wolf, "Harmonic nanocrystals for biolabeling: A survey of optical properties and biocompatibility," ACS Nano **6**(3), 2542–2549 (2012).
10. C.-L. Hsieh, R. Grange, Y. Pu, and D. Psaltis, "Three-dimensional harmonic holographic microcopy using nanoparticles as probes for cell imaging," Opt. Express **17**(4), 2880–2891 (2009).
11. J. V. Chacko, "Nanobiophotonics and fluorescence nanoscopy in 2020," in *Nano-Optics*, (Elsevier, 2020), pp. 113–162.
12. G. Popescu, *Nanobiophotonics* (McGraw-Hill, 2010).
13. Z. Wang, C. Kijatkin, A. Urban, M. Haase, M. Imlau, and K. Kömpe, "Nonlinear optical potassium niobate nanocrystals as harmonic markers: the role of precursors and stoichiometry in hydrothermal synthesis," Nanoscale **10**(22), 10713–10720 (2018).
14. L. Kocsor, L. Péter, G. Corradi, Z. Kis, J. Gubicza, and L. Kovács, "Mechanochemical reactions of lithium niobate induced by high-energy ball-milling," Crystals **9**(7), 334 (2019).
15. N.-D. Kohlenbach, C. Kijatkin, M. König, M. Haase, M. Imlau, and K. Kömpe, "The role of cations in hydrothermal synthesis of nonlinear optical sodium niobate nanocrystals," Nanoscale **12**(37), 19223–19229 (2020).
16. N. Piazza and R. Wessells, "Drosophila models of cardiac disease," in *Progress in Molecular Biology and Translational Science*, (Elsevier, 2011), pp. 155–210.
17. K. Lammers, B. Abeln, M. Hüsken, C. Lehmacher, O. E. Psathaki, E. Alcorta, H. Meyer, and A. Paululat, "Formation and function of intracardiac valve cells in the *Drosophila* heart," J. Exp. Biol. **220**(10), 1852–1863 (2017).
18. N. Doebelin and R. Kleeberg, "*Profex* : a graphical user interface for the Rietveld refinement program *BGMN*," J. Appl. Crystallogr. **48**(5), 1573–1580 (2015).
19. B. H. Toby, "R factors in rietveld analysis: How good is good enough?" Powder Diffr. **21**(1), 67–70 (2006).
20. D. Débarre, N. Olivier, W. Supatto, and E. Beaurepaire, "Mitigating phototoxicity during multiphoton microscopy of live *Drosophila* embryos in the 1.0–1.2 µm wavelength range," PLoS One **9**(8), e104250 (2014).
21. R. Schiemann, K. Lammers, M. Janz, J. Lohmann, A. Paululat, and H. Meyer, "Identification and in vivo characterisation of cardioactive peptides in drosophila melanogaster," Int. J. Mol. Sci. **20**(1), 2 (2018).
22. N. V. Kuleshov, A. A. Lagatsky, A. V. Podlipensky, V. P. Mikhailov, and G. Huber, "Pulsed laser operation of yb-doped KY(WO_4)_2 and KGd(WO_4)_2," Opt. Lett. **22**(17), 1317 (1997).
23. X. Meng, C. lv, Q. Liu, X. Zhang, Y. Li, X. Xi, and B. Zhao, "Diode-pumped yb:KGW laser with 73 fs pulse and 0.72 MW peak power based on kerr-lens mode locking," Appl. Phys. B **125**(9), 166 (2019).
24. S. Bock, C. Kijatkin, D. Berben, and M. Imlau, "Absorption and remission characterization of pure, dielectric (nano-)powders using diffuse reflectance spectroscopy: An end-to-end instruction," Appl. Sci. **9**(22), 4933 (2019).
25. C. Kijatkin, J. Eggert, S. Bock, D. Berben, L. Oláh, Z. Szaller, Z. Kis, and M. Imlau, "Nonlinear diffuse fs-pulse reflectometry of harmonic upconversion nanoparticles," Photonics **4**(4), 11 (2017).
26. J. Riporto, A. Demierre, V. Kilin, T. Balciunas, C. Schmidt, G. Campargue, M. Urbain, A. Baltuska, R. L. Dantec, J.-P. Wolf, Y. Mugnier, and L. Bonacina, "Bismuth ferrite dielectric nanoparticles excited at telecom wavelengths as multicolor sources by second, third, and fourth harmonic generation," Nanoscale **10**(17), 8146–8152 (2018).
27. Deutsche Gesetzliche Unfallversicherung, *Unfallverhütungsvorschrift Laserstrahlung, 2007*.
28. D. Jin, P. Xi, B. Wang, L. Zhang, J. Enderlein, and A. M. van Oijen, "Nanoparticles for super-resolution microscopy and single-molecule tracking," Nat. Methods **15**(6), 415–423 (2018).
29. A. Picot, S. Dominguez, C. Liu, I.-W. Chen, D. Tanese, E. Ronzitti, P. Berto, E. Papagiakoumou, D. Oron, G. Tessier, B. C. Forget, and V. Emiliani, "Temperature rise under two-photon optogenetic brain stimulation," Cell Rep. **24**(5), 1243–1253.e5 (2018).
30. C. Macias-Romero, V. Zubkovs, S. Wang, and S. Roke, "Wide-field medium-repetition-rate multiphoton microscopy reduces photodamage of living cells," Biomed. Opt. Express **7**(4), 1458 (2016).
31. E. Kim, A. Steinbrück, M. T. Buscaglia, V. Buscaglia, T. Pertsch, and R. Grange, "Second-harmonic generation of single BaTiO3 nanoparticles down to 22 nm diameter," ACS Nano **7**(6), 5343–5349 (2013).
32. C. Schmidt, J. Riporto, A. Uldry, A. Rogov, Y. Mugnier, R. L. Dantec, J.-P. Wolf, and L. Bonacina, "Multi-order investigation of the nonlinear susceptibility tensors of individual nanoparticles," Sci. Rep. **6**(1), 25415 (2016).